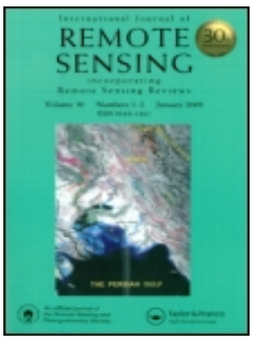

International Journal of Remote Sensing

ISSN: 0143-1161 (Print) 1366-5901 (Online) Journal homepage: http://www.tandfonline.com/loi/tres20

Detection of diurnal cycle of ocean surface wind from space-based observations

Wenqing Tang, W. Timothy Liu, Bryan Stiles & Alexander Fore

To cite this article: Wenqing Tang, W. Timothy Liu, Bryan Stiles & Alexander Fore (2014) Detection of diurnal cycle of ocean surface wind from space-based observations, International Journal of Remote Sensing, 35:14, 5328-5341, DOI: 10.1080/01431161.2014.926413

To link to this article: http://dx.doi.org/10.1080/01431161.2014.926413

International Journal of Remote Sensing, 2014
Vol. 35, No. 14, 5328–5341, http://dx.doi.org/10.1080/01431161.2014.926413

Detection of diurnal cycle of ocean surface wind from space-based observations

Wenqing Tang*, W. Timothy Liu, Bryan Stiles, and Alexander Fore

Jet Propulsion Laboratory, California Institute of Technology, Pasadena, California, USA

(*Received 14 January 2013; accepted 12 May 2013*)

We derive the diurnal cycle of ocean surface vector wind from three contemporary space-based wind sensors: OSCAT, WindSAT, and ASCAT, assuming the diurnal signal is embedded in the deviation from the daily mean as measured by ascending and descending passes of each sensor. A Monte Carlo simulation technique is used to estimate uncertainties. Strong diurnal signals are found in coastal regions and tropical oceans. Their geographical and seasonal variations are described.

1. Introduction

The large-scale diurnal variability in ocean surface wind is related to the day–night changes in a variety of elements, for example, precipitation, cloudiness, and air–sea exchanges (e.g. Lindzen and Nigam 1987; Liu and Zipser 2007; Lau, Kim, and Lee 2007; Tang and Liu 2012). It further influences climate processes such as ocean mixed-layer heat storage through diurnal forcing. Current knowledge on wind diurnal cycle is mainly based on *in situ* measurements (e.g. Deser and Smith 1998; Dai and Deser 1999), which usually have frequent temporal sampling but sparse spatial distribution. Assessments on the large-scale spatial pattern should benefit from satellite remote sensing, with a constellation of space-based wind instruments. Almost a decade ago the tandem mission of scatterometers SeaWinds on NASA QuikSCAT and Japanese Midori-2 satellites (with ascending node local crossing times at 5:54 am and 10:30 pm, respectively) provided such an opportunity. Gille, Llewellyn Smith, and Statom 2005 used six months' (April–October 2003) SeaWinds data to analyse the land/sea breeze circulation and found that diurnal wind variations propagate offshore progressively like nonlinear gravity waves and are detectable several hundreds of kilometres from the coast.

This study attempts to construct the ocean surface wind diurnal cycle using vector wind measured by three currently operational space-based wind-measuring instruments: the scatterometer on board the Indian OceanSAT-2 satellite (OSCAT), the European Advanced Scatterometer (ASCAT), and the United States Navy polarmatric radiometer WindSAT. Section 2 describes each of the three sensors and gives an assessment on the consistency of the wind data products. The methodology of deriving the wind diurnal cycle and estimating the uncertainties is given in Section 3. Results on the global and regional wind diurnal features are presented in Section 4. Finally Section 5 summarizes the results.

*Corresponding author. Email: Wenqing.Tang@jpl.nasa.gov

2. Data

Two of the three vector wind products used in this study, OSCAT and ASCAT, are retrieved from scatterometer measurements, while WindSat is a polarimetric microwave radiometer. This section gives a brief description of each sensor, examines the consistency between three products, and assesses the feasibility of combining measurements obtained from instruments of different type to construct the diurnal cycle.

A scatterometer is a microwave radar system designed to take high-precision measurements of the normalized radar cross-section (σ_o), which is sensitive to ocean surface roughness. Based on σ_o measurements within a grid cell, wind speed and direction are retrieved. OSCAT was developed by the Indian Space Research Organization (ISRO) and launched on 23 September 2009 (Chakraborty and Kumar 2013). Similar to QuikSCAT, OSCAT is a Ku-band (13.515 GHz) system with a conical scanning parabolic antenna incorporating two antenna feeds that transmit two beams of differing incidence angle and polarization, with inner beam at 49σ incidence angle of horizontal polarization (H-pol) and the outer beam at 57σ incidence of vertical polarization (V-pol), local ascending node at midnight. With a swath diameter of 1836 km, OSCAT covers about 90% of global oceans daily. The OSCAT data used in this study are processed at the Jet Propulsion Laboratory (JPL), using a technique similar to that described in Fore et al. (2012) at 12.5 km resolution with additional improvements on rain flag and rainy wind speed correction, cross-track bias adjustment, and incidence angle calibration against QuikSCAT.

ASCAT is on board the Meteorological Operational satellite programme's (MetOp) first polar-orbiting satellite (MetOp-A) launched on 19 October 2006, a joint collaboration between ESA (European Space Agency) and EUMETAT (The European Organisation for the Exploitation of Meteorological Satellites) (Figa-Saldaña et al. 2002; Bentamy and Fillon 2012). Transmitting at a frequency of 5.255 GHz (C-band), there are two sets of three antennae on each side of the satellite ground track, oriented to broadside and ±45° of broadside, making sequential observations of the backscattering of each point of interest from three directions, which are used to resolve the wind direction ambiguity. The vector wind data are retrieved for each satellite pass over a pair of 500 km-wide swaths, separated by a nadir gap approximately 700 km in width. MetOp-A has a repeat period of 29 days/412 orbits and the local equator crossing time at the ascending node is 21:30. The ASCAT wind product used in this study is 25 km resolution, downloaded from PODAAC (http://podaac.jpl.nasa.gov/OceanWind).

As an alternative to scatterometers for ocean surface wind vector measurements, WindSAT was launched on 6 January 2003 on board the Coriolis satellite, jointly sponsored by the Department of Defense Space Test Program and the US Navy. WindSat is a multi-frequency polarimetric microwave radiometer developed by the Naval Research Laboratory Remote Sensing Division and the Naval Center for Space Technology for the US Navy and the National Polar-orbiting Operational Environmental Satellite System (NPOESS) Integrated Program Office (IPO) (Gaiser et al. 2004; Yueh et al. 1999). The WindSat radiometer operates in five discrete bands – 6.8, 10.7, 18.7, 23.8, and 37.0 GHz. The 10.7, 18.7, and 37.0 GHz bands are fully polarimetric whereas the 6.8 and 23.8 GHz bands have only dual polarization. The satellite completes just over 14 orbits per day with the local equator crossing time of the ascending node at 18:00. The orbit and antenna geometry result in a forward-looking swath of approximately 1000 km and an aft-looking swath of about 350 km. The WindSAT data used in this study are the RSS (Remote Sensing System) (www.ssmi.com.windsat) version 7 product, which is the

only dataset using both the fore and aft look directions to obtain a wider swath, and with significant improvement in wind retrieval under rain. The RSS dataset consists of global binned maps on a 0.25σ × 0.25σ grid, but the effective resolution of the wind speed is 25 km × 38 km for no rain, and 39 km × 71 km in rain.

3. Methodology

Each of these wind instruments has unique capabilities and limitations. OSCAT has the best spatial coverage and resolution, but the performance of the Ku-band scatterometer degrades under rain and extremely high wind conditions, and with a cross-track bias problem; ASCAT is less susceptible to rain contamination at the C-band, but with narrower swaths and coarse measurement resolution, and its accuracy seems to degrade at low wind speeds whereas WindSAT was developed based on very different remote-sensing technology. The consistency between the three datasets was examined by bin-averaging the data along swath from the corresponding source on a uniform 1σ × 1σ grid at a monthly time scale or longer. Figures 1 and 2 show the fields of the zonal (U) and meridional (V) wind speeds for JJA (June, July, and August) 2011, and DJF (December, January, and February) 2011–2012, respectively, except that the June 2012 data of OSCAT were used for JJA due to the current availability of OSCAT data from July 2011 to July 2012. Considering the very different nature of instruments as described above and summarized in Table 1, the monthly and seasonal maps created from three data products showed excellent agreement, both on global feature and seasonal contrast. In the

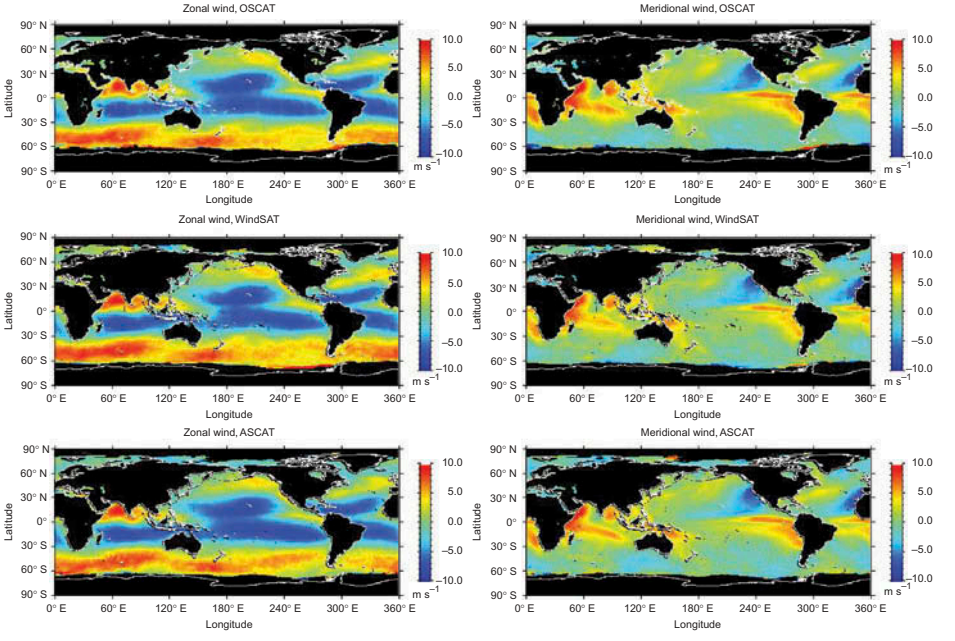

Figure 1. Mean fields of zonal (left) and meridional (right) wind composed over three months (June, July, and August) from three independent instruments: OSCAT (top), WindSAT (middle), and ASCAT (bottom).

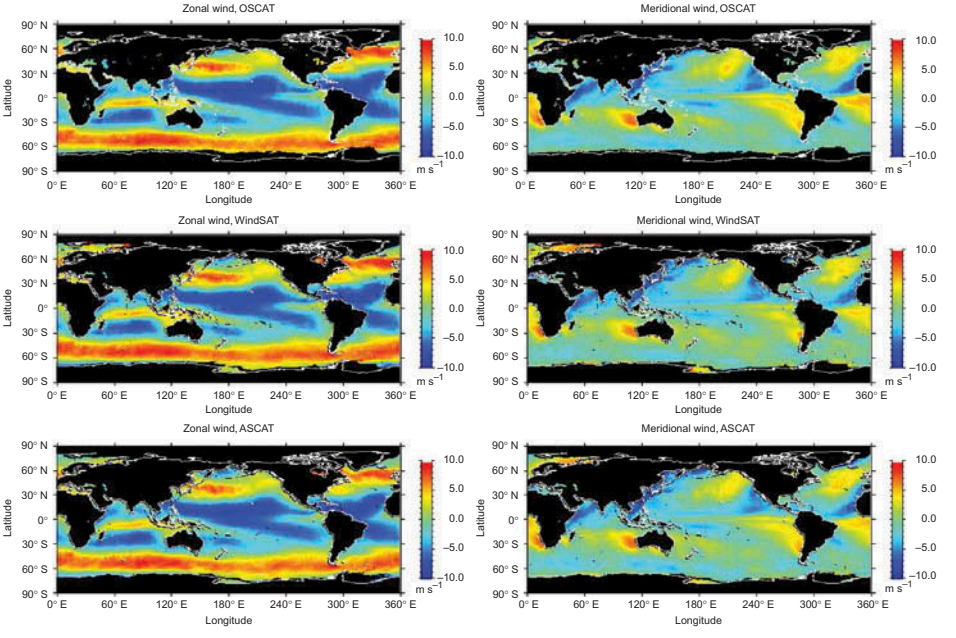

Figure 2. As Figure 1, but for December, January, and February.

Table 1. Instrument specifications.

	OceanSat-2	ASCAT	WindSAT
Instrument	Scatterometer	Scatterometer	Polarimetric radiometer
Frequency (GHz)	13.515	5.255	6.8, 10.7, 18.7, 23.8, and 37.0
Swath width (km)	1836	Two 500 swaths separated by a nadir gap of 700	1000
Local time at ascending node	0:00	21:30	18:00

ideal case of absolute removal of biases between sensors, the deviation from the common base captured by different sensors at different local times should give the signal on the diurnal variation.

However, as shown more clearly in Figure 3 for the longitudinally averaged profiles of wind components, discrepancies do exist between products especially at high latitudes. Based on the assumption that each wind sensor self-consistently detects the diurnal cycle, we choose to focus on the ascending/descending deviation from each sensor's daily mean, and therefore the approach of this study does not require absolute removal of biases between sensors. Separately averaging data collected by ascending and descending passes from OSCAT, ASCAT, and WindSAT, and removing the daily mean, we obtain six global maps corresponding to two local passing times for each satellite. Figures 4 and 5 show the zonal wind deviation from the daily mean in time order centred at 0:00, 6:00, 9:30, 12:00, 18:00, and 21:30 local time, averaged over three months for JJA and DJF, respectively. Similar deviation maps for the meridional wind component are given in Figures 6 and 7.

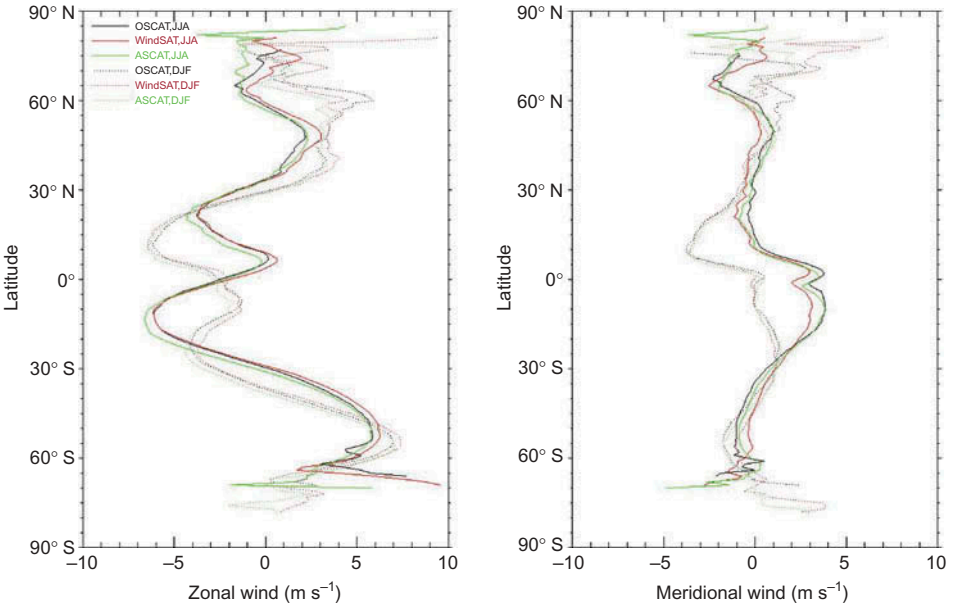

Figure 3. Longitudinally averaged (left) zonal and (right) meridional wind for JJA (solid) and DJF (dotted) for OSCAT (black), WindSAT (red), and ASCAT (green).

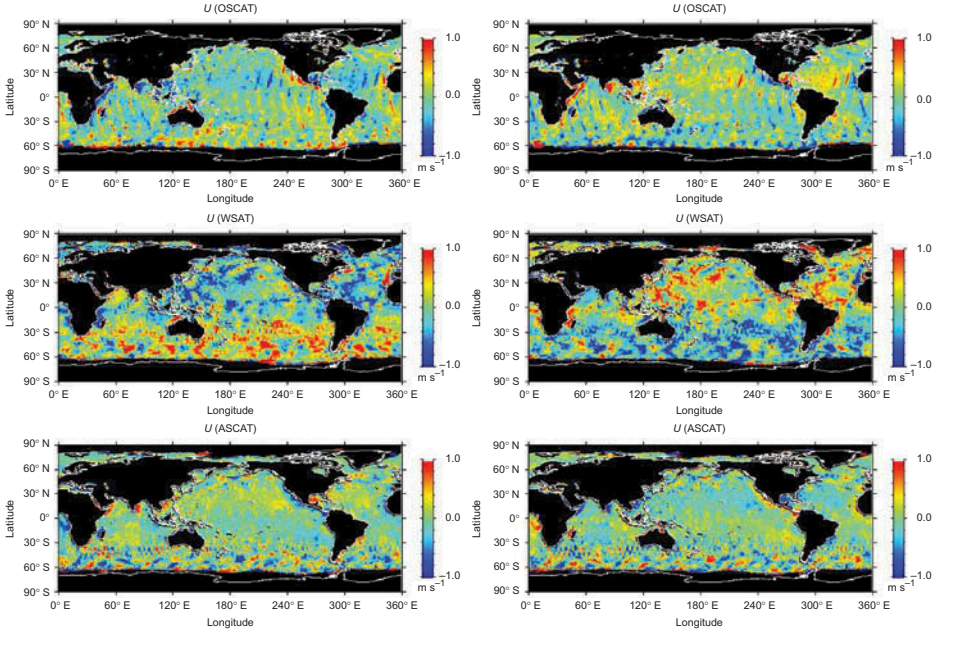

Figure 4. Zonal wind component deviation from daily mean of morning (left) and evening (right) passes for OSCAT (top), WindSAT (middle), and ASCAT (bottom), averaged over June, July, and August.

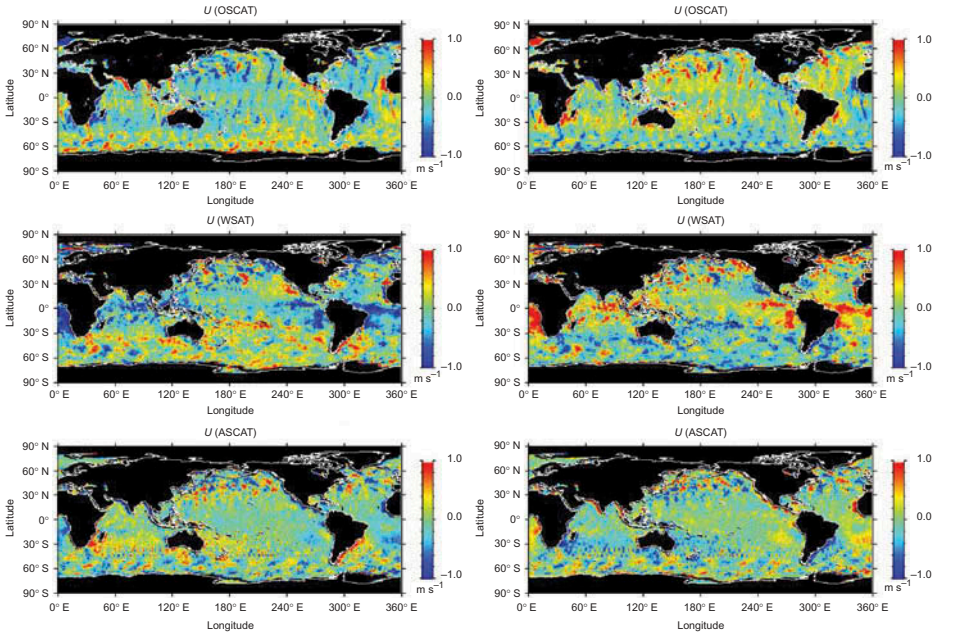

Figure 5. As Figure 4, but for December, January, and February.

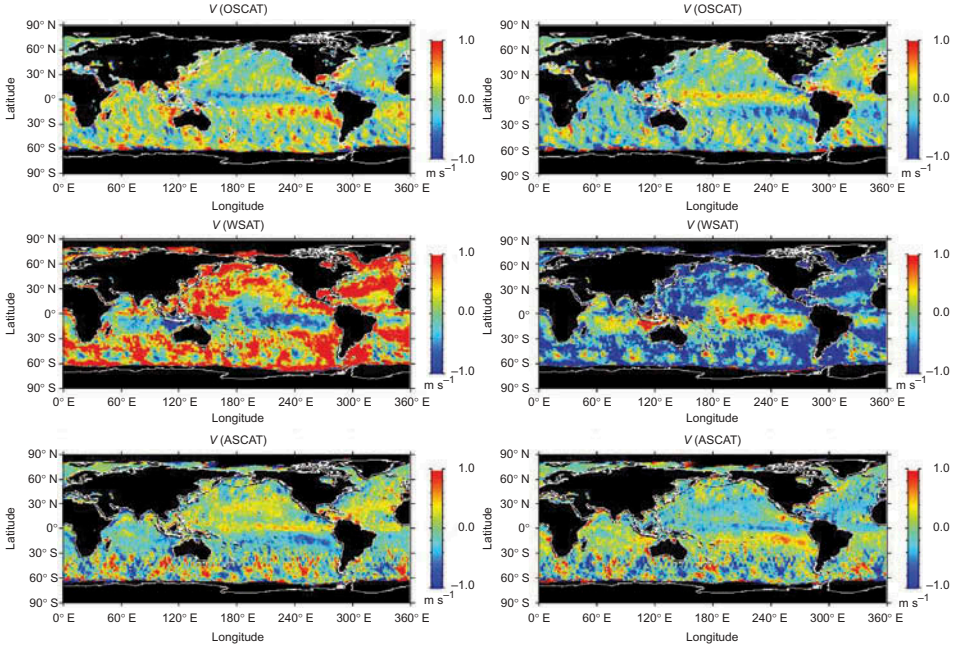

Figure 6. Meridional wind component deviation from daily mean of morning (left) and evening (right) passes for OSCAT (top), WindSAT (middle), and ASCAT (bottom).

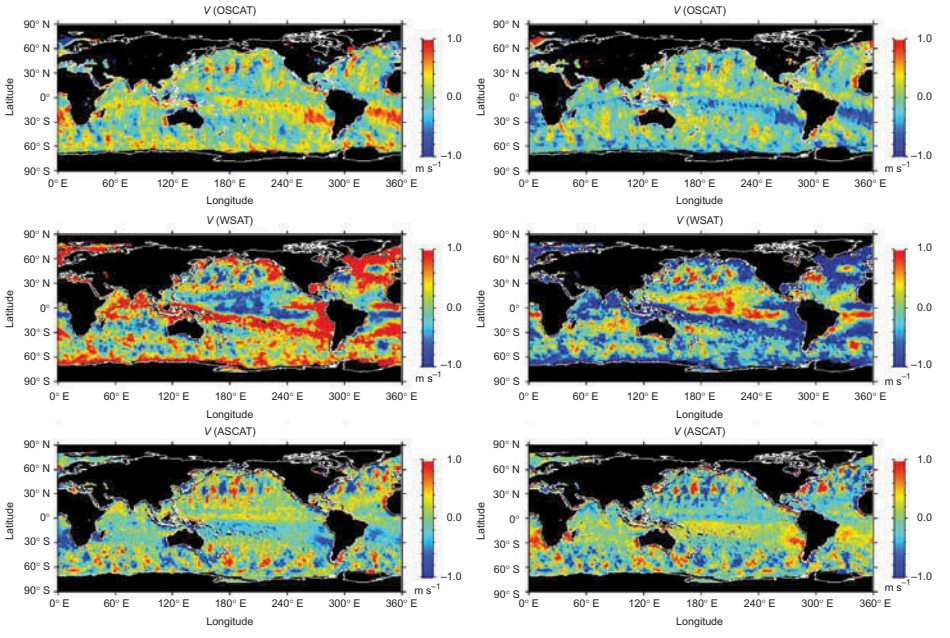

Figure 7. As Figure 6, but for December, January, and February.

Although the three wind products depict similar large-scale features in daily mean and its seasonal changes (Figures 1 and 2), the diurnal signal embedded in the deviation of ascending and descending passes from the daily mean shows different patterns for JJA and DJF (Figures 4–7). Generally speaking, in the coastal area where diurnal cycle is dominated by sea breezes, due to the nature of sea breezes caused by day/night differential heating over land and ocean, winds are expected to be more offshore in the morning and more onshore in the evening, relative to the daily mean.

We construct the diurnal cycle for U and V by fitting the six data values to the first-order harmonic:

$$X(t) = A_1 \sin(2\pi t/24 + P_1 + \varepsilon, \tag{1}$$

where X denotes U or V, A_1 is the amplitude, P_1 is the phase of the diurnal cycle, t is the local time in hours (0 − 24), and ε represents uncertainty due to unresolved higher-order variation. The following outlines detail procedures as well as the Monte Carlo simulation technique used to estimate the uncertainties.

(a) For each sensor, calculate mean U and V on a global $1\sigma \times 1\sigma$ grid over the selected period (monthly or seasonal; JJA and DJF were used in this study).
(b) Calculate twice-daily mean and standard deviation for each sensor with ascending and descending passes separated and daily mean from (a) removed.
(c) On each grid point, fit the six data values from (b) to Equation (1) to obtain the amplitude A_1 and phase P_1 of the diurnal cycles.

(d) Replace X by perturbed values, which are obtained by adding to the original six data values random numbers with a Gaussian distribution and a variance equivalent to the standard error of the time-averaged means; then re-derive A_1 and P_1.
(e) Repeat (d) 100 times for the Monte Carlo simulation of uncertainty analysis.
(f) The uncertainties in A_1 and P_1 can be assessed from the standard deviations, δ_{A1} and $\delta_{P1,}$ computed from the 100 realizations of A_1 and P_1 obtained from the noise-added data set.

4. Results

Figure 8 depicts the amplitude of the diurnal cycle (A_1) of U and V for JJA and DJF, respectively. The data are masked out (white) if A_1 is less than twice the standard deviation, $2\delta_{A1}$, an arbitrary criterion used to filter out insignificant signals. The most dominant feature is that significant large diurnal amplitudes are observed in coastal regions, with interesting seasonal contrast in most of these regions. For example, in the Bay of Bengal off India and in the South China Sea off Vietnam (Figure 9(*a*)), both zonal and meridional A_1 is much higher in JJA (boreal summer) than in DJF (boreal winter). These contrasts may reflect the stronger diurnal character of the summer monsoon. Significant A_1 in both zonal and meridional wind is observed along the North America coast and in the Gulf of Mexico (Figure 9(*b*)), but with less seasonal contrast. Along the west coast of Africa (Figure 9(*c*)), in the southern hemisphere, the zonal A_1 in the austral summer DJF is stronger than in JJA (austral winter). In South America (Figure 9(*d*)), the strong zonal A_1 along the east coast from Brazil to Argentina in DJF completely

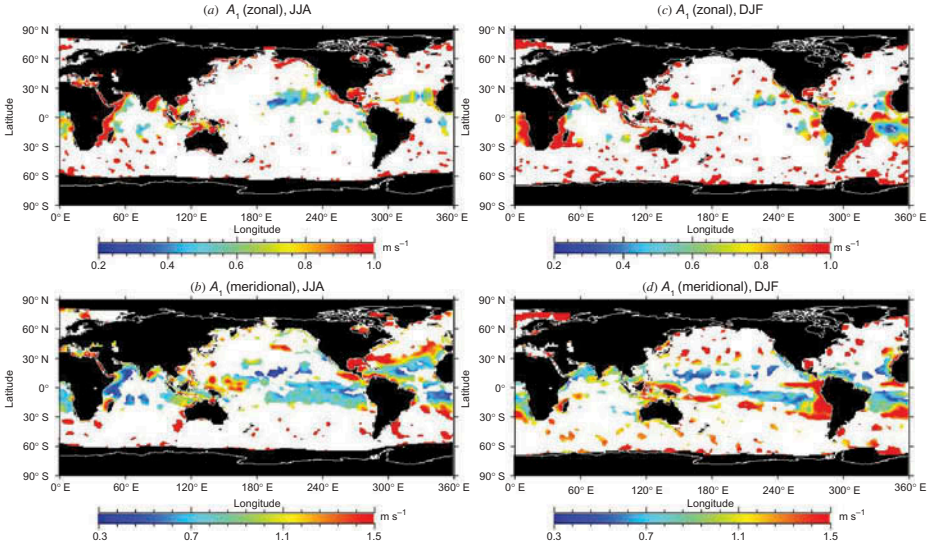

Figure 8. Amplitude of the diurnal cycle, A_1, of zonal (upper panel) and meridional (lower panel) wind components for JJA (left) and DJF (right). White areas mask out locations where A_1 is less than twice the standard deviation of $A_{1.}$

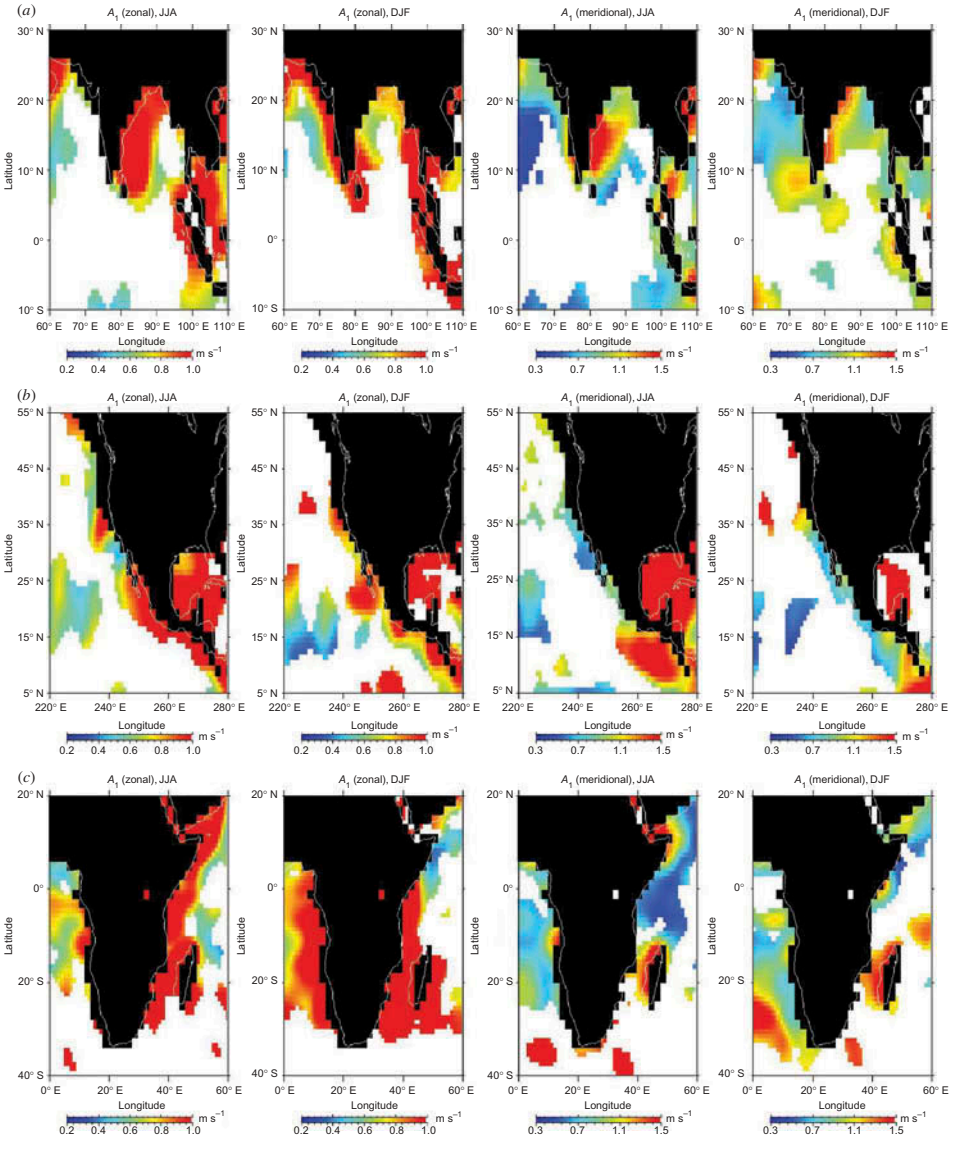

Figure 9. (*a*) Similar to Figure 8, magnified for regions near India and Southeast Asia. (*b*) Similar to Figure 8, magnified for the North American west coast and the Gulf of Mexico. (*c*) Similar to Figure 8, magnified for the African coast. (*d*) Similar to Figure 8, magnified for the east coast of South America. (*e*) Similar to Figure 8, magnified for the tropical Pacific Ocean. (*f*) Similar to Figure 8, magnified for the tropical Atlantic Ocean.

disappears in JJA while the meridional A_1 on the northern coast of South America is stronger in the boreal summer than in winter. Near the west coast of South America (Figure 9(*e*)), a very strong meridional A_1 is observed extending to thousands of kilometres westward into the tropical Pacific Ocean in DJF, when the mean meridional circulation is weaker (ref. Figures 1 and 2). Patterns of strong meridional A_1 are observed

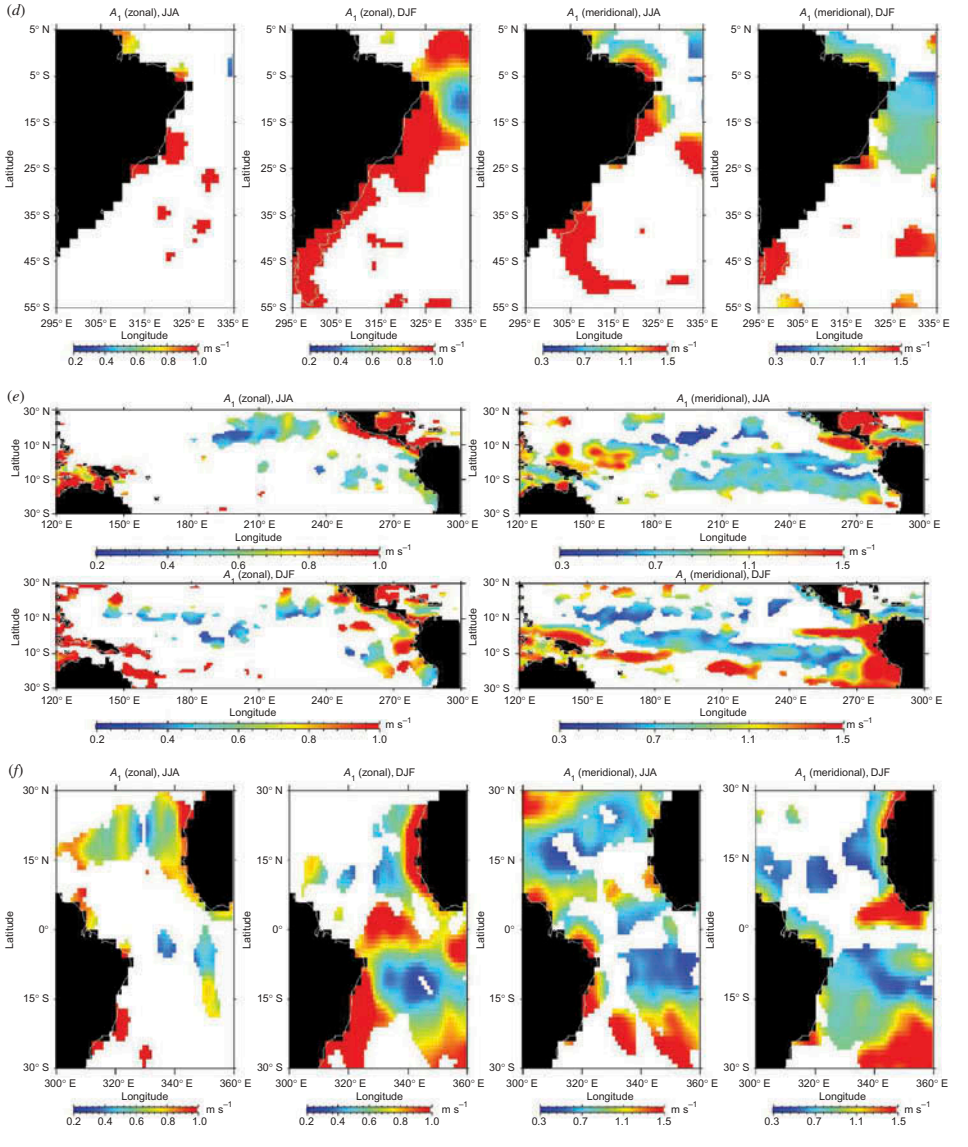

Figure 9. (Continued).

in the tropical Atlantic (Figure 9(*f*)) and Pacific (Figure 9(*e*)) in both seasons, while only a weak zonal A_1 is observed in the tropical Atlantic in DJF. Beyond the tropics, no coherent pattern can be found in the open oceans.

The phase of the diurnal cycle (P_1) in terms of local time when the cycle peaks, with A_1 larger than $2\delta_{A1}$, is shown in Figure 10. P_1 in regions where significant seasonal contrast was observed in A_1 (Figure 9) are shown in Figure 11. Because the diurnal cycle is a harmonic, the first (positive) peak will be followed by another negative peak 12 hours later. Examining zonal and/or meridional wind components relative to the

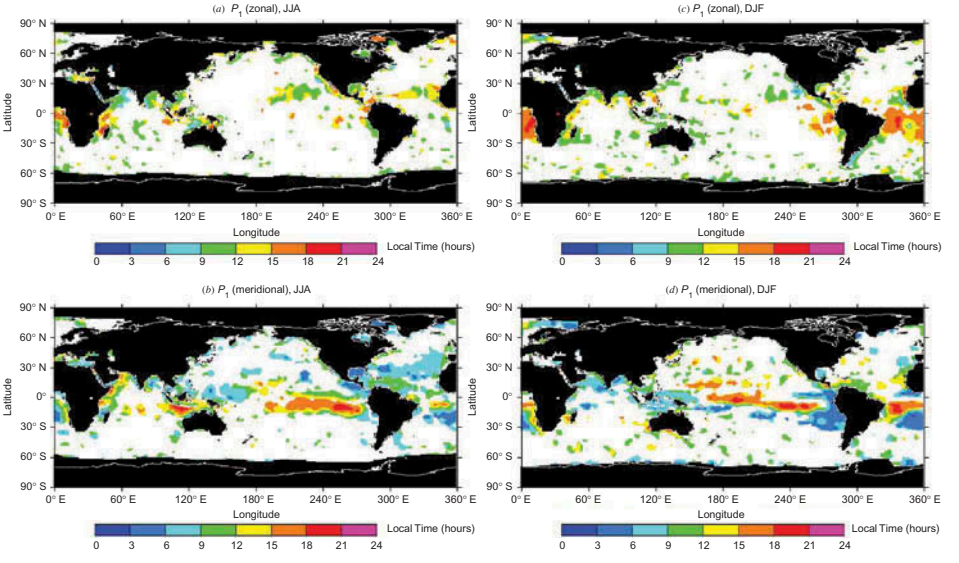

Figure 10. Phase of the diurnal cycle, P_1, of zonal (upper panel) and meridional (lower panel) wind components for JJA (left) and DJF (right), shown as local time when the diurnal cycle peaks, with white area masked out where A_1 is less than twice the standard deviation of A_1.

regional orientation of coastlines, we discerned the characteristics of land–sea breezes in coastal regions. For example, along the Oregon/California coast in JJA, the eastward (onshore) wind peaks in the evening at 18:00 (orange); along the eastern coasts of Brazil and Argentina in DJF, the zonal wind P_1 is around 6:00–9:00 (green, cyan), which means that the westward onshore component peaks in the evening around 18:00–21:00. In the Bay of Bengal, India, the offshore zonal component peaks in the morning. Of course exceptions exist – for example, along the western coast of South America where the orographic effect may dominate. In open oceans, zonally coherent large-scale patterns can only be found in the tropics, where meridional winds tend to be more northward late in the evening over the Inter-Tropical Convergence Zone (ITCZ), and peak progressively earlier away from the equator, while zonal winds appear to be more eastward in the evening (orange, red) in large area south of the equator in the Atlantic Ocean in DJF.

5. Summary

The diurnal cycle of wind components was derived from vector wind products of the constellation of two scatterometers and one polarimetric radiometer. The results reveal strong diurnal signals along the coast associated with sea breezes in tropical oceans associated with deep convections. The results also suggest seasonal variation in the diurnal cycle. A comparison between the diurnal variation of surface wind convergence and rain rate will reveal the influence of deep convection, which will be demonstrated in a follow-up paper. We also indicate that wind data accuracy improvements are particularly necessary in low-wind speed areas – for example, over

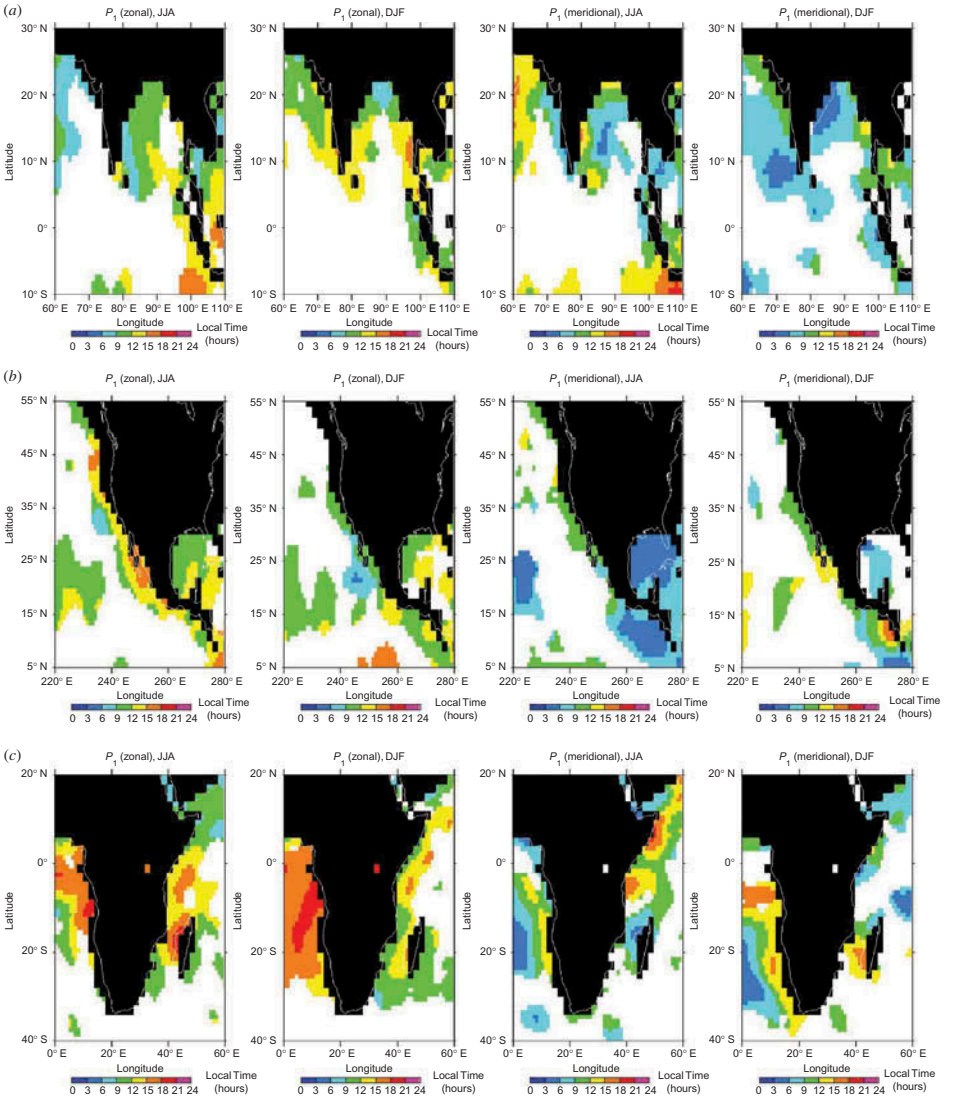

Figure 11. (*a*) Similar to Figure 10, magnified for India and Southeast Asia. (*b*) Similar to Figure 10, magnified for the west coast of North America and the Gulf of Mexico. (*c*) Similar to Figure 10, magnified for the coast of Africa. (*d*) Similar to Figure 10, magnified for the east coast of South America. (*e*) Similar to Figure 10, magnified for the tropical Pacific Ocean. (*f*) Similar to Figure 10, magnified for the tropical Atlantic Ocean.

equatorial ITCZ – from the perspective of linking wind convergence with surface precipitation on the diurnal scale.

Acknowledgement

The work described in this paper was carried out at the Jet Propulsion Laboratory, California Institute of Technology under a contract with the National Aeronautics and Space Administration.

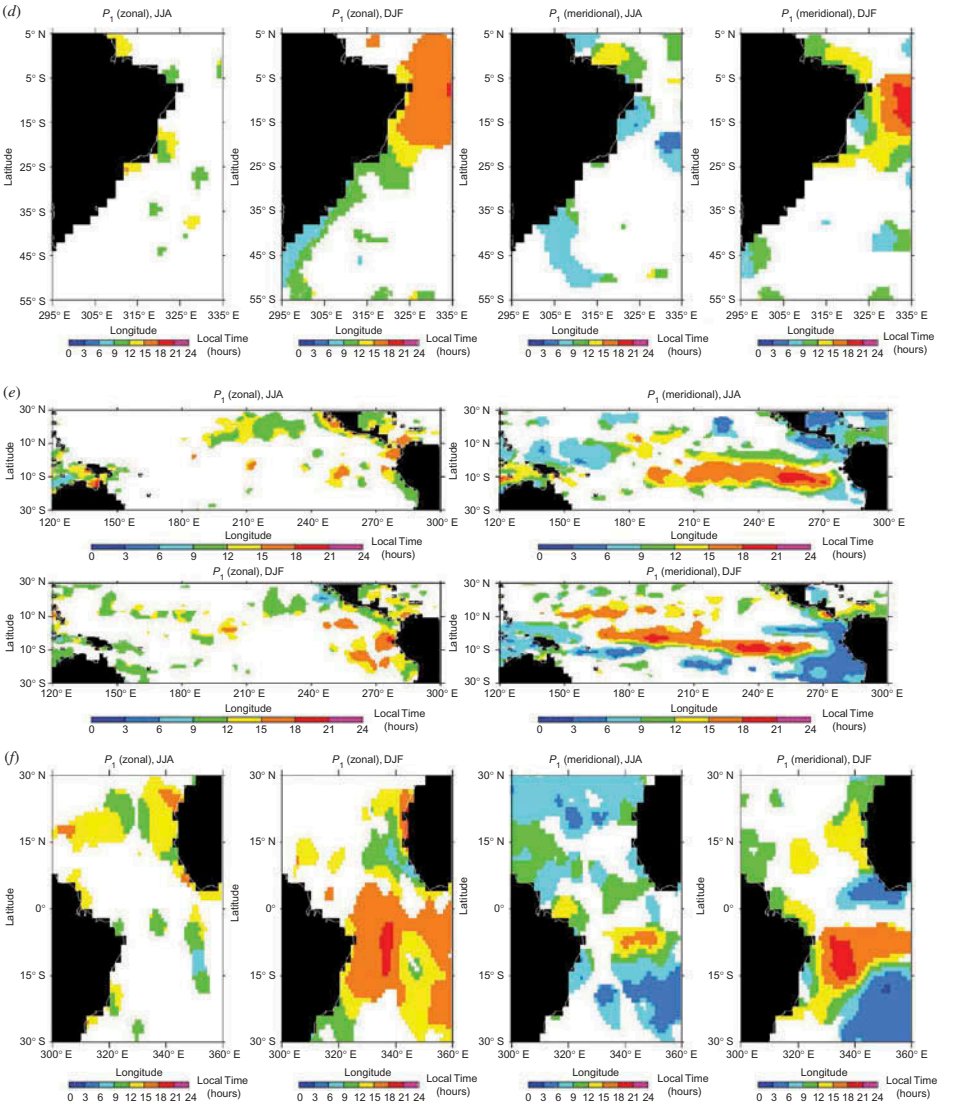

Figure 11. (Continued).

References

Bentamy, A., and D. C. Fillon. 2012. "Gridded Surface Wind Fields from Metop/Ascat Measurements." *International Journal of Remote Sensing* 33: 1729–1754. doi:10.1080/01431161.2011.600348.

Chakraborty, A., and R. Kumar. 2013. "Generation and Validation of Analysed Wind Vectors over the Global Oceans." *Remote Sensing Letters* 4 (2): 114–122. doi:10.1080/2150704X.2012.701344.

Dai, A., and C. Deser. 1999. "Diurnal and Semidiurnal Variations in Global Surface Wind and Divergence Fields." *Journal of Geophysical Research* 104 (D24): 31109–31125. doi:10.1029/1999JD900927.

Deser, C., and C. A. Smith. 1998. "Diurnal and Semidiurnal Variations of the Surface Wind Field over the Tropical Pacific Ocean." *Journal of Climate* 11: 1730–1748. doi:10.1175/1520-0442(1998)011<1730:DASVOT>2.0.CO;2.

Figa-Saldaña, J., J. J. W. Wilson, E. Attema, R. Gelsthorpe, M. R. Drinkwater, and A. Stoffelen. 2002. "The Advanced Scatterometer (ASCAT) on the Meteorological Operational (Metop) Platform: A Follow on for European Wind Scatterometers." *Canadian Journal of Remote Sensing* 28 (3): 404–412. doi:10.5589/m02-035.

Fore, A. G., B. W. Stiles, A. H. Chau, B. A. Williams, R. S. Dunbar, and W. Rodrigues. 2012. "Point-wise Wind Retrieval and Ambiguity Removal Improvements for the Quikscat Climatological Data Set." *IEEE Transactions on Geoscience and Remote Sensing* 52 (1): 51–59. doi:10.1109/TGRS.2012.2235843.

Gaiser, P. W., K. M. Germain St, E. M. Twarog, G. A. Poe, W. Purdy, D. Richardson, W. Grossman, W. L. Jones, D. Spencer, G. Golba, J. Cleveland, L. Choy, R. M. Bevilacqua, and P. S. Chang. 2004. "The Windsat Spaceborne Polarimetric Microwave Radiometer: Sensor Description and Early Orbit Performance." *IEEE Transactions on Geoscience and Remote Sensing* 42 (11): 2347–2361. doi:10.1109/TGRS.2004.836867.

Gille, S. T., S. G. Llewellyn Smith, and N. M. Statom. 2005. "Global Observations of the Land Breeze." *Geophysical Research Letters* 32: L05605. doi:10.1029/2004GL022139.

Lau, W. K. M., K.-M. Kim, and M.-I. Lee. 2007. "Characteristics of Diurnal and Seasonal Cycles in Global Monsoon Systems." *Journal of the Meteorological Society of Japan* 85A: 403–416. doi:10.2151/jmsj.85A.403.

Lindzen, R. S., and S. Nigam. 1987. "On the Role of Sea Surface Temperature Gradients in Forcing Low-Level Winds and Convergence in the Tropics." *Journal of Atmospheric Sciences* 44: 2418–2436. doi:10.1175/1520-0469(1987)044<2418:OTROSS>2.0.CO;2.

Liu, C., and E. J. Zipser. 2007. "Diurnal Cycles of Precipitation, Clouds, and Lightning in the Tropics from 9 Years of TRMM Observations." *Geophysical Research Letters* 35: L04819. doi:10.1029/2007GL032437.

Tang, W., and W. T. Liu. 2012. "Relating Ocean Surface Wind and Rain." Accessed May 31, 2014. https://ams.confex.com/ams/92Annual/webprogram/Paper198715.html

Yueh, S. H., W. J. Wilson, S. Dinardo, and F. K. Li. 1999. "Polarimetric Microwave Brightness Signatures of Ocean Wind Directions." *IEEE Transactions on Geoscience and Remote Sensing* 37 (2): 949–959. doi:10.1109/36.752213.